Biomaterials Science

ROYAL SOCIETY OF CHEMISTRY

PAPER

View Article Online
View Journal

Cite this: DOI: 10.1039/d6bm00733c

Advanced 3D-printed PLA scaffolds functionalized with dual small molecules for enhanced bone regeneration: *in vitro* and *in vivo* studies

Nisa İrem Büyük, [a] Ezgi Hacıhasanoğlu, [b] Çağla Çiçek [c] and Gamze Torun Köse *[a]

Bone defects remain a significant clinical challenge due to limited vascularization and insufficient osteogenesis. In this study, 3D-printed PLA scaffolds functionalized with dual small molecule-loaded chitosan nanoparticles containing DIPQUO and GS4012 (DG-NP-coated scaffolds) were developed to support osteogenic and angiogenic responses. Representative physicochemical characterization confirmed successful nanoparticle coating, nanoscale particle distribution, and sustained release behavior of the incorporated small molecules. *In vitro* analyses demonstrated enhanced osteogenic differentiation of rat bone marrow mesenchymal stem cells cultured on DG-NP-coated scaffolds, with increased ALP activity, calcium deposition, and osteogenic gene expression. Notably, ONC expression reached a 54.19-fold increase by day 21. *In vitro* co-culture studies additionally demonstrated enhanced endothelial cell migration on GS4012-containing scaffold surfaces. *In vivo* evaluation in a critical-sized rat calvarial defect model revealed enhanced bone tissue formation and the presence of vascularized tissue regions in DG-NP-coated scaffolds compared to untreated and uncoated groups, with a bone mineral density of 757 mg HA cm^{-3} at week 8. Collectively, these findings suggest that DG-NP functionalized PLA scaffolds represent a promising bioactive platform for supporting vascularized bone regeneration in bone tissue engineering applications.

Received 9th May 2026,
Accepted 20th June 2026

DOI: 10.1039/d6bm00733c

rsc.li/biomaterials-science

1. Introduction

Bone tissue disorders, including fractures, osteoporosis, and degenerative diseases, represent a significant global health burden, affecting millions of individuals annually.[1] Current therapeutic strategies, such as autografts, allografts, and synthetic implants, are limited by donor site morbidity, immune rejection, and insufficient integration with native tissues.[2] Therefore, there is an urgent need for advanced biomaterials and tissue engineering approaches to overcome these limitations effectively.

The field of tissue engineering has seen increasing interest in the use of three-dimensional (3D) printed scaffolds for bone regeneration.[3] These scaffolds offer the ability to precisely control the architecture and composition, thereby tailoring their properties to the specific needs of the target tissue. Polylactic acid (PLA), a biodegradable and biocompatible polymer, is widely utilized in 3D-printed scaffolds due to its tunable mechanical properties and ease of processing.[4] Additionally, these scaffolds can be designed with specific pore sizes, porosities, and mechanical properties to mimic the structure and function of native bone tissue. However, the inherent hydrophobicity and limited bioactivity of PLA necessitate surface modification strategies to enhance cellular interactions and promote tissue regeneration.

To further enhance the functionality of 3D-printed PLA scaffolds, incorporating bioactive agents, such as small molecules and growth factors, has been identified as a valuable strategy. Chitosan, a natural polysaccharide-based delivery system, has been explored for this purpose due to its improved stability, biocompatibility, and targeted delivery capabilities.[5,6] Previous studies have demonstrated the potential of chitosan nanoparticle-based delivery systems for osteogenic and angiogenic bioactive agents in enhancing bone regeneration and vascularization.[7,8]

Building upon our previous studies, in which the structural optimization of 3D-printed PLA scaffolds and the development of dual small molecule-loaded chitosan nanoparticles were investigated independently,[9,10] the present study aimed to evaluate the combined biological performance of these two optimized

[a]*Department of Genetics and Bioengineering, Faculty of Engineering, Yeditepe University, Istanbul, Türkiye. E-mail: nirembuyuk@gmail.com, gamzekose@yeditepe.edu.tr; Tel: +90216 5780000-1617*
[b]*Department of Pathology, Yeditepe University, Istanbul, Türkiye. E-mail: ezgi.hacihasanoglu@saglik.gov.tr*
[c]*Department of Plastic, Reconstructive and Aesthetic Surgery, Kartal Dr Lütfi Kırdar City Hospital, Istanbul, Türkiye. E-mail: caglamutkan2002@gmail.com*

platforms within a single scaffold system. While the previous studies established the engineering and drug delivery aspects separately, their integration into a multifunctional scaffold and subsequent validation through both *in vitro* osteogenic and angiogenic assays as well as an *in vivo* critical-sized bone defect model have not previously been investigated. In this study, surface modification of 3D-printed PLA scaffolds was achieved to introduce reactive hydroxyl (OH) groups, creating a bioactive interface conducive to further functionalization.[11] Following surface modification, chitosan nanoparticles were synthesized and employed as carriers for therapeutic agents. Specifically, dual small molecule-loaded chitosan nanoparticles were fabricated by incorporating DIPQUO and GS4012 to target osteogenic differentiation and angiogenesis, respectively. Some nanoparticles were left unloaded, while others were loaded with either DIPQUO, GS4012, or a combination of both, providing a biofunctional platform for localized small molecule delivery. The coordinated support of osteogenesis and vascularization is critical for effective bone regeneration, as both processes contribute to tissue integration and defect healing.[12]

This study presents a nanoparticle-functionalized 3D-printed PLA scaffold system designed to support osteogenic and angiogenic responses through the combined delivery of DIPQUO and GS4012. By integrating surface-modified PLA scaffolds with dual small molecule-loaded chitosan nanoparticles, the developed platform was evaluated through both *in vitro* and *in vivo* analyses to investigate its potential for vascularized bone regeneration.

2. Materials and methods

2.1. Fabrication and surface modification of 3D-printed PLA scaffolds

PURASORB® PL 10 (Corbion) polylactic acid (PLA) beads were melt-extruded into 1.75 mm diameter filaments using a twin-screw extruder prior to FDM fabrication. The resulting filaments exhibited stable extrusion behavior during scaffold fabrication, enabling reproducible printing of the designed scaffold architecture. PLA scaffolds were fabricated using a commercial fused deposition modeling 3D printer (X1 3D printer, Zaxe, Turkey). A three-dimensional cylinder model with a diameter of 10 mm and a height of 2.5 mm was employed in STL format. A 60% infill rate was selected, as this architecture was previously shown to provide suitable porosity and mechanical properties for bone tissue engineering applications.[9]

To improve surface bioactivity and facilitate nanoparticle immobilization, the PLA scaffolds were subjected to alkaline surface treatment. Briefly, scaffolds were immersed in 0.5 M NaOH solution at 37 °C for 4 h under gentle agitation to partially hydrolyze ester bonds and introduce hydroxyl (–OH) groups onto the scaffold surface. Following treatment, the scaffolds were thoroughly rinsed with deionized water until neutral pH was achieved and subsequently dried overnight in a vacuum oven at 37 °C.

2.2. Synthesis of chitosan nanoparticles and loading with small molecules

Chitosan nanoparticles (NPs) were synthesized using the ionic gelation method under previously optimized conditions.[10] DIPQUO and GS4012 were incorporated into the nanoparticles *via* passive loading during nanoparticle formation. Blank nanoparticles, DIPQUO-loaded nanoparticles (D-NP, 3.15 μgmL^{-1}), GS4012-loaded nanoparticles (G-NP, 10 μgmL^{-1}), and dual-loaded nanoparticles (DG-NP) were prepared.

The physicochemical properties of the nanoparticles, including particle size distribution, morphology, surface charge, and release behavior, were characterized as previously described.[10]

2.3. Coating of scaffolds with chitosan nanoparticles

The overall fabrication and coating strategy of the scaffold system is schematically illustrated in Fig. 1A. Surface-modified PLA scaffolds were coated with chitosan nanoparticles *via* dip coating. Prior to coating, nanoparticle suspensions were diluted 1 : 20 in sterile deionized water based on preliminary optimization studies to improve cytocompatibility and coating homogeneity. Scaffolds were immersed in the nanoparticle suspensions and placed under vacuum overnight to facilitate nanoparticle penetration and surface attachment. Coated scaffolds were subsequently dried and stored at 4 °C until further use.

The experimental groups used throughout the study are summarized in Table 1.

2.3.1. Characterization of scaffolds. The morphology and surface characteristics of the fabricated scaffolds were examined using scanning electron microscopy (SEM; Carl Zeiss EVO, Germany). SEM imaging was performed to evaluate scaffold architecture, surface morphology before and after alkaline treatment, and the presence of nanoparticle coatings on the scaffold surface. The mechanical properties of the 3D-printed PLA scaffolds were evaluated as previously described (Fig. S1).[9]

To assess scaffold stability and degradation behavior, *in vitro* degradation and enzymatic degradation studies were performed under physiological conditions, and the corresponding weight loss, swelling behavior, and pH changes were monitored over time (Fig. S2).

2.4. *In vitro* evaluation

Rat bone marrow mesenchymal stem cells (rBMSCs) were used for all *in vitro* experiments. Cells were cultured in Dulbecco's modified Eagle's medium (DMEM-low; Gibco, Thermo Fisher Scientific, Waltham, MA, USA) supplemented with 10% fetal bovine serum (FBS) and 1% penicillin–streptomycin. Cells were maintained at 37 °C in a humidified atmosphere with 5% CO_2.

2.4.1. Cell viability-cytotoxicity and proliferation assay. Cell viability on the scaffolds was assessed using the MTS assay (CellTiter 96® AQueous One Solution, Promega). On days 7,

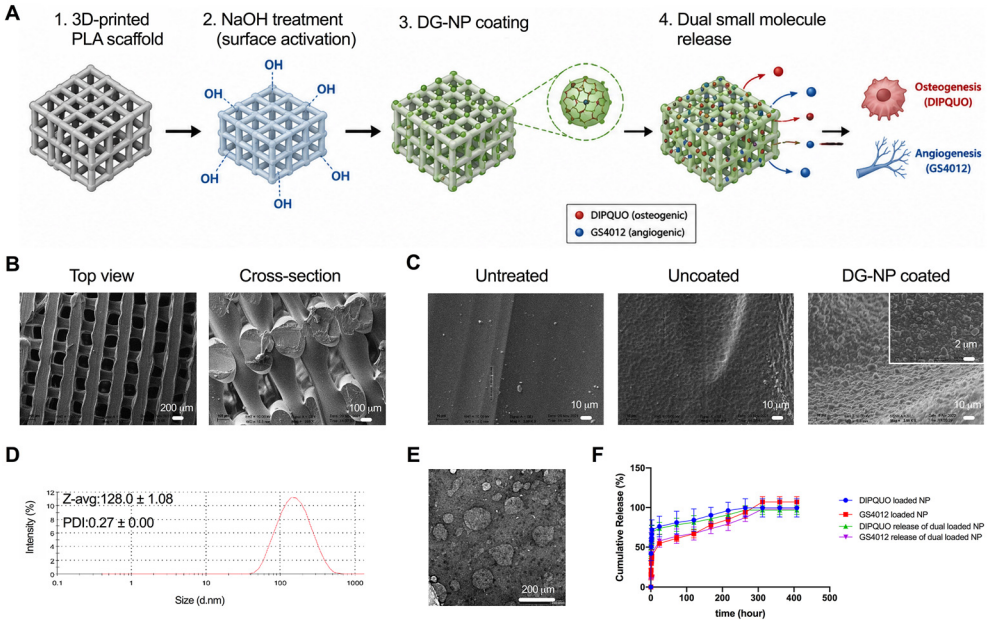

Fig. 1 Representative physicochemical characterization of the DG-NP functionalized PLA scaffold platform. (A) Schematic illustration of the fabrication and functionalization process of 3D-printed PLA scaffolds. (B) SEM images of the 3D-printed PLA scaffold architecture showing top-view and cross-sectional morphology of the 60% infill scaffold. (C) SEM micrographs of untreated PLA, alkali-treated (uncoated) PLA, and DG-NP coated scaffold surfaces. (D) Particle size distribution of DG-NPs determined by dynamic light scattering (DLS). (E) TEM image of DG-NPs demonstrating nanoparticle morphology. (F) *In vitro* cumulative release profiles of DIPQUO and GS4012 from single- and dual-loaded chitosan nanoparticles over time.

Table 1 Experimental groups

Sample	Conditions
Untreated	PLA scaffold
Uncoated	Alkali treated PLA scaffold
Blank coated	Alkali treated PLA scaffold + blank NP
D-NP coated	Alkali treated PLA scaffold + D-NP
G-NP coated	Alkali treated PLA scaffold + G-NP
DG-NP coated	Alkali treated PLA scaffold + DG-NP

14, and 21, the MTS reagent was added to the culture medium, and absorbance was measured at 490 nm using a microplate reader (Varioskan Lux, Thermo Scientific).

Cell proliferation was evaluated using the PicoGreen assay (Quant-iT™ PicoGreen™ dsDNA Assay Kit, Thermo Fisher Scientific). DNA content was quantified at days 7, 14, and 21 by measuring fluorescence (excitation: 480 nm; emission: 520 nm).

Live and dead cells on the scaffolds were visualized using a live/dead staining kit (L3224, Thermo Fisher Scientific). Cells were stained with calcein-AM and ethidium bromide, and images were captured using a fluorescence microscope (VertA1, Zeiss, Germany).

2.4.2. Osteogenic differentiation analysis. Osteogenic differentiation of rBMSCs on the scaffolds was induced by culturing cells in osteogenic differentiation medium (OM, DMEM-low glucose supplemented with 100 nM dexamethasone, 10 mM β-glycerophosphate, and 50 μg mL^{-1} ascorbic acid-2-phosphate with 10% FBS and 100 μ mL^{-1} penicillin–streptomycin) for 21 days. Every 3 days, fresh OM was added, and the rBMSCs were incubated for 7, 14, and 21 days. At the end of each time point, osteogenic analysis and characterizations were carried out.

Differentiation was evaluated by the following assays:

- **ALP activity:** ALP activity was measured using SIGMAFAST™ *p*-Nitrophenyl Phosphate Tablets (N2770, Sigma-Aldrich). Absorbance was read at 405 nm.
- **Calcium deposition:** calcium content was quantified using the QuantiChrom™ Calcium Assay Kit (DICA-500, BioAssay Systems). Absorbances were measured at 612 nm. The Ca^{2+} concentration in the medium was determined by the calibration curve.
- **Osteocalcin expression:** osteocalcin levels were measured using the Rat Gla-Osteocalcin High Sensitive EIA Kit (MK126, Takara) and the Rat Glu-Osteocalcin High Sensitive EIA Kit (MK146, Takara) according to the manufacturer's instructions. Absorbances were measured at 450 nm.
- **Staining:** mineralization was visualized using von Kossa staining (Diagnostic Biosystems, KT028-IFU, USA) and Alizarin Red Solution (2003999, Merck).
- **Gene expression analysis:** real-time PCR (RT-PCR) was performed to quantify osteogenic gene expression. RNA was extracted using the easy-spin™ Total RNA Extraction Kit (Intron), and cDNA synthesis was carried out using the iScript cDNA Synthesis Kit (Bio-Rad). Gene-specific primers targeting osteogenic markers (Table 2) were used for amplification with Maxima SYBR Green qPCR Master Mix (Thermo Fisher

Table 2 Sequences of the primers used for the quantitative PCR

Primers		Sequence (5′→3′)
Osteonectin	F	CACTGGCTGTGTTGGAAACG
	R	GTGGAGGAGACAGCAAGGTC
Runx2	F	TCACTACCAGCCACCGAGAC
	R	ACGCCATAGTCCCTCCTTTT
Collagen type I	F	GCCTGCACA TGTGTGGCCG
	R	CTGCCCCTCGCAGGGGTTT

Scientific) using the CFX96 Touch™ Real-Time PCR Detection System. Relative gene expression levels were normalized to GAPDH as the housekeeping gene and calculated relative to the uncoated scaffold group.

2.4.3. *In vitro* angiogenesis study. To evaluate the angiogenic potential of the scaffolds, an *in vitro* co-culture model was employed. Immunofluorescence (IF) staining was used to monitor the migration of rat peripheral blood endothelial cells (rPBECs) onto the scaffold surfaces under different nanoparticle coating conditions. Red fluorescent-stained rBMSCs were seeded onto the scaffolds at a density of 50 000 cells per scaffold. Separately, green fluorescent-stained rPBECs were seeded into Transwell inserts (0.8 μm pore size) at a density of 50 000 cells per insert. After 24 h, the inserts were placed over the scaffold cultures to initiate co-culture. Scaffold surfaces were imaged on days 3, 7, and 14 using a fluorescence microscope to evaluate endothelial cell migration and distribution.

2.5. *In vivo* evaluation

All animal experiments were approved by the Yeditepe University Experimental Research Center (YUDETAM) under protocol number 2020-848 and conducted in accordance with institutional ethical guidelines. Male Sprague–Dawley rats (8 weeks old) were used for *in vivo* studies. Critical-sized calvarial defects (8 mm diameter) were surgically created under anesthesia, and scaffolds (untreated, uncoated, and DG-NP coated) were implanted into the defect sites. The surgical area was subsequently closed with sutures. *In vivo* analyses were performed using $n = 6$ animals per group.

2.5.1. Histological analysis. Explanted calvarial tissues were fixed in 10% neutral buffered formalin, processed using a Leica ASP6025 automated tissue processor, and embedded in paraffin. Sections (4 μm thickness) were stained with hematoxylin and eosin (H&E) and Masson's trichrome to evaluate tissue integration, new bone formation, connective tissue distribution, and vascularized tissue regions.

2.5.2. Micro-computed tomography (μCT) analysis. Bone regeneration was monitored using μCT imaging (μCT-50, Scanco Medical Inc., Switzerland) at weeks 4 and 8 post-implantation. The volume of new bone formation was quantified using μCT analysis software.

2.6. Statistical analysis

Statistical analyses were performed using GraphPad Prism software (GraphPad Software, USA). Data were analyzed using one-way analysis of variance (ANOVA) followed by Tukey's *post hoc* test for multiple comparisons. A p-value lower than 0.05 was considered statistically significant. Unless otherwise stated, *in vitro* experiments were performed with $n = 3$ samples per group, while *in vivo* experiments were conducted using $n = 6$ animals per group.

3. Results

3.1. Morphological and structural analysis of scaffolds

The fabrication and functionalization strategy of the scaffold system is schematically illustrated in Fig. 1A. The morphological characteristics of the 3D-printed PLA scaffolds with a 60% filling rate were evaluated by SEM analysis (Fig. 1B). The scaffolds exhibited a uniform and interconnected porous architecture conducive to cell infiltration and nutrient diffusion. ImageJ analysis revealed an average top-view pore diameter of 464.30 ± 10.60 μm and a cross-sectional pore size of 346.46 ± 26.46 μm. The scaffold porosity, calculated gravimetrically, was 43.8%, consistent with the designed scaffold architecture.

SEM analysis demonstrated a relatively smooth surface morphology in untreated PLA scaffolds, whereas alkali treatment increased surface roughness (Fig. 1C). Following nanoparticle coating, DG-NP deposition was observed on the scaffold surface (Fig. 1C), indicating successful surface coating.

Representative characterization data[10] of DG-NPs are presented in Fig. 1D–F. DLS analysis demonstrated nanoscale particle distribution with a Z-average size of 128.0 ± 1.08 nm, a PDI of 0.27 ± 0.00, and a positive zeta potential of 18.0 ± 0.74 mV. Encapsulation efficiencies of DIPQUO and GS4012 in DG-NPs were determined as 79.37 ± 13.84% and 75.15 ± 10.95%, respectively. TEM analysis confirmed spherical nanoparticle morphology, while *in vitro* release analysis demonstrated distinct release profiles of DIPQUO and GS4012 over time. The optimized 60% infill PLA scaffold exhibited adequate mechanical performance for bone tissue engineering applications. Comprehensive mechanical characterization, including compressive modulus, compressive strength at yield, compressive strength at break, tensile modulus, ultimate tensile strength, and fracture strength, is presented in Fig. S1. Selected characterization data were adapted and reorganized from our previous studies.[9,10]

3.2. *In vitro* evaluation

3.2.1. Cell viability-cytotoxicity and proliferation assays. Following preliminary optimization of the nanoparticle coating concentration (Fig. S3), the cytocompatibility of NP-coated scaffolds was evaluated using MTS, PicoGreen, and live/dead assays. The optimization study demonstrated that higher nanoparticle coating concentrations reduced cell viability, whereas a 1 : 20 dilution restored cell viability to a level comparable to the uncoated scaffold. Therefore, the 1 : 20 dilution was selected for all subsequent biological experiments.

MTS assay results (Fig. 2A) demonstrated low cell viability in uncoated and untreated scaffolds across all time points.

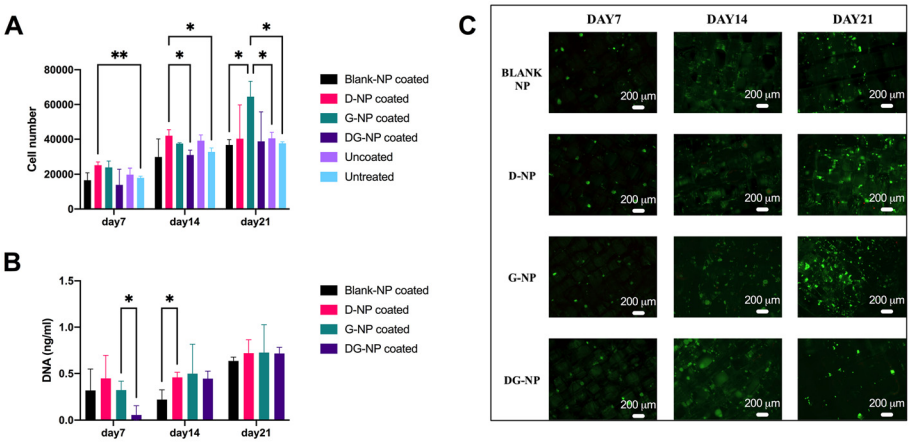

Fig. 2 (A) MTS assay of rBMSC-seeded scaffolds where cells were seeded at a density of 5×10^4 in DMEM growth medium; $n = 3$, $p < 0.05$, (B) cell proliferation assay (PicoGreen) of rBMSC-seeded scaffolds; $n = 3$, $p < 0.05$, (C) rBMSC viability in 3D-printed PLA scaffolds by live-dead staining throughout 7, 14, and 21 days of incubation (dead cells: red; live cells: green), scale bar: 200 μm.

D-NP-coated scaffolds showed significantly higher viability than untreated scaffolds after 7 and 14 days; however, this difference was no longer observed by day 21. At the end of day 21, G-NP-coated scaffolds exhibited significantly higher cell viability compared to non-DIPQUO-containing groups.

Cell proliferation, assessed *via* the PicoGreen assay (Fig. 2B), revealed a consistent increase in DNA content over time across all groups. On day 7, G-NP-coated scaffolds exhibited significantly higher DNA levels compared to DG-NP-coated scaffolds. By day 14, D-NP-coated scaffolds showed higher DNA content compared to blank NP-coated scaffolds. By day 21, DNA levels continued to increase, although differences between scaffold types were not statistically significant.

Live/dead staining (Fig. 2C) visualized cell adhesion, spreading, and growth on NP-coated scaffolds. Fluorescence microscopy demonstrated increasing cell density over time in all groups. On day 21, G-NP-coated scaffolds exhibited enhanced cell spreading and interconnections between scaffold pores.

3.2.2. Osteogenic differentiation of rBMSCs. The osteogenic potential of rBMSCs cultured on NP-coated scaffolds was evaluated through ALP activity, calcium deposition, osteocalcin secretion, and osteogenic gene expression analyses.

ALP activity results (Fig. 3A) demonstrated a decrease after day 7 in all groups except the blank NP-coated scaffolds. Blank NP- and DG-NP-coated scaffolds exhibited significantly higher ALP activity compared to the other groups throughout the 21-day culture period. Calcium quantification results (Fig. 3B) revealed progressive calcium accumulation over time, with significantly higher calcium levels observed in D-NP-coated scaffolds on day 7. However, no statistically significant differences were detected between groups by day 21.

Osteocalcin (OCN) secretion was evaluated in two forms: Gla-OCN, associated with bone remodeling, and Glu-OCN, associated with cellular energy metabolism (Fig. 3C). Gla-OCN levels increased progressively throughout the culture period, particularly in DIPQUO-containing groups. In contrast, Glu-OCN levels were elevated in DG-NP-coated scaffolds.

Alizarin red staining (Fig. 3D) demonstrated progressive calcium deposition over time, with more prominent mineral accumulation observed in D-NP- and DG-NP-coated scaffolds by day 21. Similarly, von Kossa staining (Fig. 3E) confirmed enhanced mineralized matrix formation in NP-containing groups.

Gene expression analysis of ONC, Runx2, and Col1a1 (Fig. 3F) demonstrated time-dependent increases in osteogenic marker expression. ONC expression was initially higher in blank NP-coated scaffolds but was surpassed by D-NP- and DG-NP-coated scaffolds by day 21. Runx2 expression progressively increased throughout the culture period, with the highest fold change observed in G-NP-coated scaffolds at day 21. Col1a1 expression was more pronounced in DIPQUO-containing scaffolds, with the highest expression detected in DG-NP-coated scaffolds at the final time point.

3.2.3. Angiogenic potential. The migration of rPBECs from Transwell inserts onto the surface of rBMSC-seeded scaffolds was evaluated during a 14-day co-culture period. Representative immunofluorescence images demonstrated progressive endothelial cell migration and adhesion on scaffold surfaces over time (Fig. 4A). Green fluorescent-labeled rPBECs were observed on all scaffold groups; however, their presence was more pronounced on G-NP-coated scaffolds, particularly at later time points.

To further assess endothelial cell migration, green fluorescence-positive area (%) was quantified as an indicator of endothelial coverage on scaffold surfaces (Fig. 4B). Quantitative analysis revealed a time-dependent increase in endothelial coverage in all groups. At day 7, G-NP-coated scaffolds exhibited significantly greater endothelial coverage compared with Blank NP-coated scaffolds ($p < 0.05$). By day 14, endothelial coverage on G-NP-coated scaffolds was significantly higher than both Blank NP-coated and uncoated

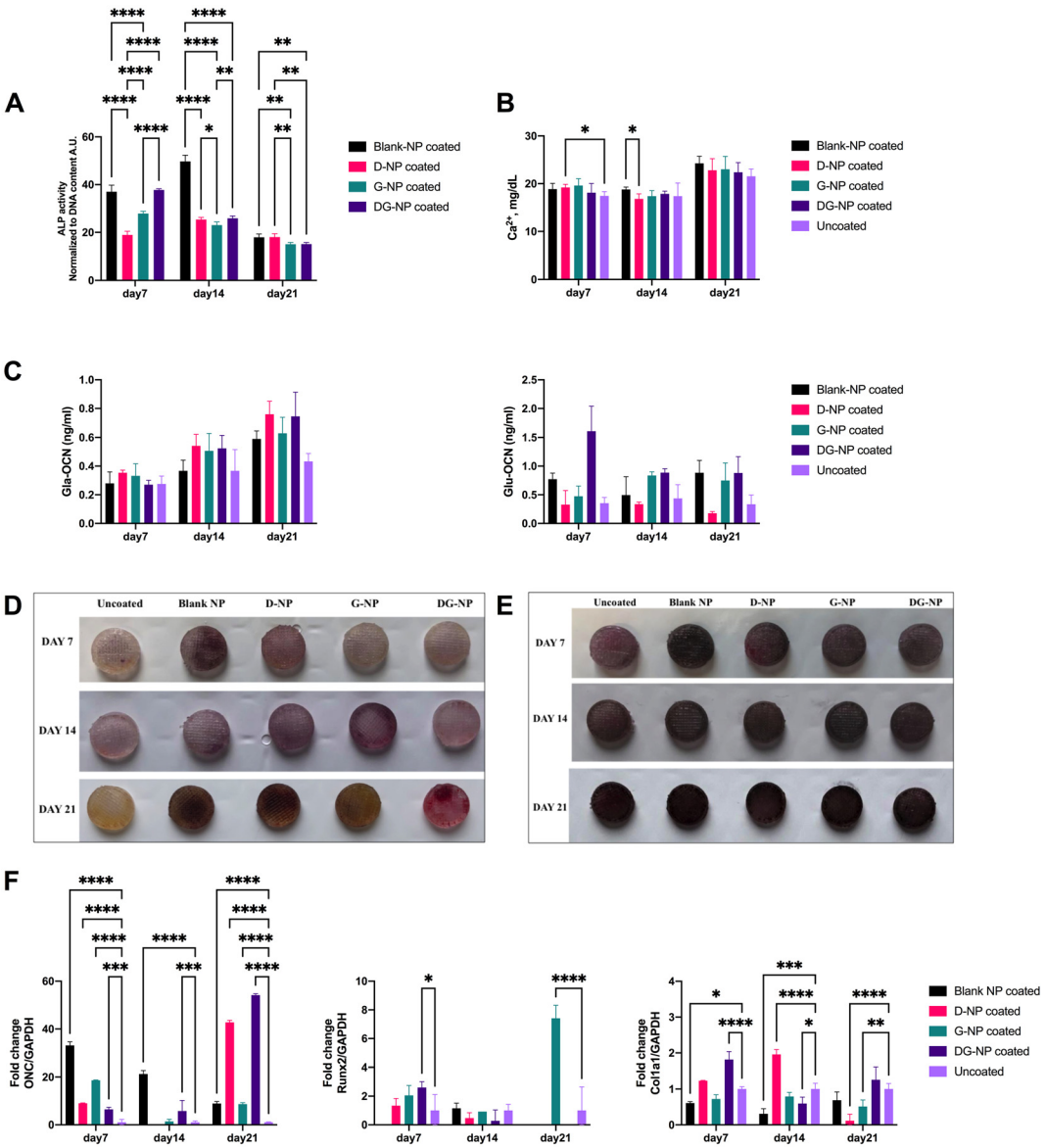

Fig. 3 Osteogenic differentiation of rBMSCs cultured on NP-coated scaffolds for 7, 14, and 21 days evaluated by (A) ALP analysis (the data were normalized against DNA content), (B) calcium assay, (C) osteocalcin assay: Gla-OCN and Glu-OCN, respectively, (D) Alizarin red staining, (E) von Kossa staining, and (F) ONC, Runx2, and Col1a1 gene expression analysis; $n = 3$, $p < 0.05$.

scaffolds ($p < 0.05$). Although Blank NP-coated scaffolds also supported endothelial cell migration, likely due to the presence of chitosan nanoparticles, GS4012-containing scaffolds demonstrated the highest endothelial coverage throughout the culture period.

3.3. *In vivo* evaluation

To evaluate the effect of scaffold functionalization on bone regeneration, histological and micro-CT analyses were performed at 4 and 8 weeks post-implantation. As illustrated in Fig. 5A, critical-sized calvarial defects were created, followed by implantation of untreated, uncoated, or DG-NP-coated scaffolds.

Masson's trichrome staining was performed to evaluate connective tissue and newly formed bone tissue within the defect area (Fig. 5B). At 4 weeks post-implantation (Fig. 5B; a1–c1), connective tissue was predominantly observed in all groups. By week 8 (Fig. 5B; a2–c2), more pronounced bone tissue formation was detected in the DG-NP-coated scaffold group compared to the untreated and uncoated groups.

Histopathological evaluation of H&E-stained sections further demonstrated differences in tissue regeneration between groups (Fig. 5C). In the untreated group (Fig. 5C; a1, a2, b1, and b2), connective tissue predominated, with limited bone tissue formation detected throughout the study period. The uncoated scaffold group (Fig. 5C; c1, c2, d1, and d2) demonstrated moderately increased bone tissue formation compared to the untreated group. In contrast, the DG-NP-coated scaffold group (Fig. 5C; e1, e2, f1, and f2) exhibited

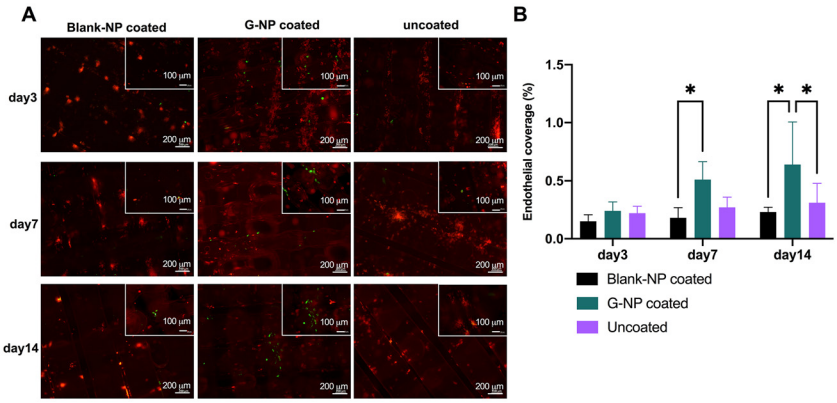

Fig. 4 *In vitro* angiogenic evaluation of scaffold groups. (A) Representative immunofluorescence images showing migration of green fluorescent-labeled rPBECs onto red fluorescent-labeled rBMSC-seeded scaffold surfaces following co-culture at days 3, 7, and 14. Scale bars: 200 μm; inset scale bars: 100 μm. (B) Quantitative analysis of endothelial coverage (%) determined from green fluorescence-positive area measurements; $n = 3$, $p < 0.05$.

more extensive bone tissue formation, increasing from 40% at week 4 to 70% at week 8 (Fig. 5D). Histological observations additionally revealed more prominent vascularized tissue regions in the DG-NP-coated scaffold group relative to the untreated and uncoated groups.

Micro-CT analysis demonstrated enhanced bone regeneration in DG-NP-coated scaffolds compared to untreated and uncoated scaffolds at both time points (Fig. 5F). Newly formed bone tissue was more evident in the DG-NP-coated group at week 4 and further increased by week 8. Bone mineral density measurements supported these observations, demonstrating significantly higher bone density values in the DG-NP-coated scaffold group at the final time point (Fig. 5E).

Overall, these findings suggest that DG-NP functionalization promoted enhanced bone tissue regeneration and supported the formation of vascularized tissue within the defect area.

4. Discussion

To enhance scaffold functionality and promote stable nanoparticle adhesion, PLA was surface-modified to facilitate NP attachment, since its inert and hydrophobic nature limits direct integration.[13] A mild alkaline treatment (0.5 M NaOH) was applied to partially hydrolyze ester bonds, introducing hydroxyl groups on the surface while maintaining mechanical integrity.[14] Similar approaches have been reported using NaOH-treated PLA scaffolds coated with chitosan nanoparticles for enhanced osteogenic responses,[15] highlighting the effectiveness of surface modification in promoting cell attachment and proliferation. SEM analysis confirmed the presence of nanoparticle deposition on the scaffold surface following the immersion coating process. This surface modification was intended to facilitate nanoparticle attachment while also increasing surface hydrophilicity, potentially improving cell–scaffold interactions, consistent with previous findings on NaOH-treated PLA scaffolds.[16,17] The degradation behavior of the scaffold system may additionally contribute to the observed regenerative response. While PLA provides long-term structural stability, chitosan nanoparticles exhibit comparatively faster degradation and release behavior, supporting early-stage bioactive molecule delivery. This difference in degradation profiles may support sustained scaffold integrity while allowing localized biological stimulation during the initial phases of bone healing.

NP-coated scaffolds were evaluated for cell interactions, beginning with cell viability and attachment analyses. Undiluted chitosan nanoparticles initially exhibited cytotoxicity, likely due to their nanoscale dimensions and positively charged surfaces, which can disrupt cell membranes, as also noted in previous reports on cationic nanomaterials.[18] To address this, nanoparticles were diluted 1 : 20 prior to coating, substantially improving cell compatibility and attachment, consistent with earlier findings on optimized chitosan surface treatments.[19] Following this adjustment, MTS and live-dead assay results confirmed time-dependent increases in cell viability and proliferation, demonstrating that the coating process preserved scaffold biocompatibility. GS4012-coated scaffolds showed a time-dependent proliferation advantage, while DIPQUO-loaded NPs also exhibited improved cytocompatibility, which may be associated with the controlled release characteristics of the nanoparticle delivery system. Moreover, SEM analysis demonstrated the presence of nanoparticle deposition on the scaffold surface together with well-spread rBMSCs exhibiting typical fibroblast-like morphology. These results indicate that the nanoparticle coating not only provided surface bioactivity but also supported favorable cell–material interactions. Overall, the developed system provided a cytocompatible nanoparticle-functionalized scaffold suitable for subsequent biological evaluation and *in vivo* assessment.

Osteogenic differentiation was assessed through ALP activity, calcium deposition, and gene expression analyses. ALP activity peaked on day 14, particularly in blank NP and

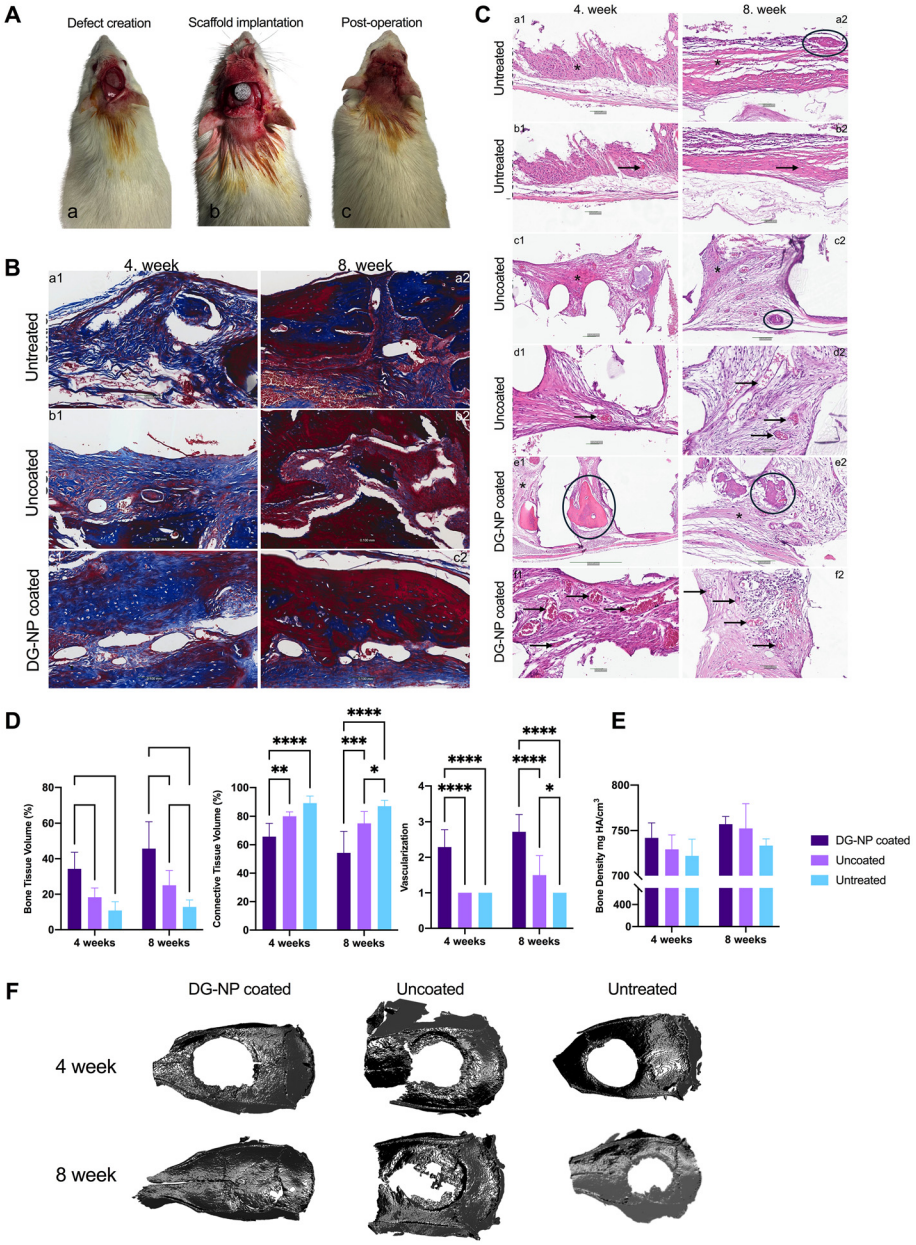

Fig. 5 *In vivo* evaluation of bone regeneration in the critical-sized calvarial defect model. (A) Representative images of the surgical procedure, including creation of the critical-sized calvarial defect, scaffold implantation, and closure of the surgical site. (B) Masson's trichrome-stained sections of untreated, uncoated, and DG-NP-coated scaffold groups at 4 and 8 weeks post-implantation. Increased bone tissue formation was observed in the DG-NP-coated scaffold group at week 8 compared to the untreated and uncoated groups. (C) Hematoxylin and eosin (H&E)-stained sections of untreated, uncoated, and DG-NP-coated scaffold groups at 4 and 8 weeks post-implantation. Connective tissue (asterisk), bone tissue (circle), and vascularized tissue regions (arrow) are indicated. (D) Histological quantification of bone tissue, connective tissue, and vascularized tissue regions in each experimental group. (E) Bone mineral density (BMD) values obtained from micro-CT analysis at 4 and 8 weeks post-implantation. (F) Representative micro-CT reconstructed images demonstrating bone regeneration in untreated, uncoated, and DG-NP-coated scaffold groups at 4 and 8 weeks post-implantation. Data are presented as mean ± SD (n = 6, $p < 0.05$).

DG-NP-coated scaffolds, likely reflecting chitosan's osteoinductive properties.[20] Calcium assay results aligned with the literature,[21–23] demonstrating consistent calcium deposition. Gla-OCN, a bone remodeling marker, increased over time, particularly in DIPQUO-containing groups, while Glu-OCN, related to energy metabolism, was elevated in dual-molecule groups. Although the biological significance of this observation requires further investigation, the increased Glu-OCN levels may reflect differences in osteoblast maturation. Alizarin red and von Kossa staining confirmed calcium deposition and mineralization, with the highest differentiation observed in DIPQUO-containing scaffolds. Real-time PCR analysis of ONC,

Runx2, and Col1a1 gene expression further supported the osteogenic response observed *in vitro*. Runx2, an early transcription factor crucial for osteoblast differentiation, was significantly upregulated at day 7 in DG-NP coated scaffolds, indicating accelerated osteogenic commitment.[24,25] In contrast, ONC, a late marker, increased markedly over time, especially in DIPQUO-containing groups, consistent with enhanced mineralization reported in previous studies.[26] The progressive rise in Col1a1 expression from day 14 to day 21 also aligns with its role in matrix formation and maturation during bone regeneration.[12,24,25] Collectively, these data indicate that DIPQUO-functionalized scaffolds support a progressive osteogenic differentiation, promoting both early osteoblast commitment and late-stage mineral deposition. The combined delivery system supported osteogenic differentiation more effectively than uncoated scaffolds.

Considering the critical role of vascularization in bone regeneration,[12,27,28] the effects of GS4012 on endothelial cell behavior were evaluated using an *in vitro* co-culture model. GS4012, a known VEGF-inducing small molecule,[29] showed higher efficacy when delivered *via* NPs than through direct medium application, which highlights the advantage of controlled release strategies reported in previous studies.[30,31] Immunofluorescence analysis demonstrated the presence of rPBECs on all scaffold groups throughout the culture period. In addition to qualitative observations, quantitative image analysis revealed significantly greater endothelial coverage on G-NP-coated scaffolds compared with Blank NP-coated scaffolds at day 7 and compared with both Blank NP-coated and uncoated scaffolds at day 14. Chitosan nanoparticles alone also supported endothelial cell attachment and coverage, which is consistent with previous reports describing favorable endothelial interactions with chitosan-based materials.[32] Collectively, these findings suggest that the incorporation of GS4012 contributed to enhanced endothelial cell coverage on scaffold surfaces under the experimental conditions evaluated in this study. These findings further support the importance of combining osteogenic and endothelial cues within a single scaffold platform, as vascularization plays a critical role in successful bone tissue regeneration.[10,12,27,33]

In vivo, DG-NP coated scaffolds significantly promoted bone regeneration relative to uncoated and untreated scaffolds, as demonstrated by histological and micro-CT analyses. Masson's trichrome and H&E staining revealed increased bone tissue formation, organized collagen deposition, and early vascularization in the DG-NP group, particularly at 4 weeks, which became more pronounced by 8 weeks, indicating progressive defect repair. These observations were corroborated by micro-CT measurements, showing significantly higher bone volume and density in the coated scaffolds at both time points. The incorporation of DIPQUO and GS4012 likely contributed to these effects by promoting osteoblast differentiation and endothelial responses, consistent with previous studies.[10,26,34,35] The progressive increase in bone density and tissue organization points to the role of scaffold functionalization and bioactive coatings in accelerating defect repair, aligning with findings from Wulandari *et al.*[36] and Chen *et al.*[11] Overall, these results suggest that DG-NP-coated scaffolds supported enhanced bone regeneration and vascularized tissue formation, highlighting their potential for bone tissue engineering applications.

Building upon the previously optimized scaffold architecture and nanoparticle delivery platform,[9,10] the present findings demonstrate that their integration into a single scaffold supports both osteogenic and endothelial responses while improving bone regeneration *in vivo*. Together, these findings provide biological validation of the integrated scaffold platform in a preclinical critical-sized calvarial defect model and highlight its potential for vascularized bone tissue engineering.

Conclusion

In this study, dual small molecule-loaded chitosan nanoparticles containing DIPQUO and GS4012 were successfully integrated onto 3D-printed PLA scaffolds to develop a multifunctional platform for bone tissue engineering applications. The DG-NP-coated scaffolds supported rBMSC viability, osteogenic differentiation, and endothelial cell migration *in vitro*, while *in vivo* analyses demonstrated enhanced bone tissue formation and the presence of vascularized tissue regions compared to untreated and uncoated scaffolds.

The combined delivery of osteogenic and angiogenic small molecules through a nanoparticle-functionalized scaffold system represents a promising strategy for supporting vascularized bone regeneration. Collectively, these findings highlight the potential of DG-NP functionalized PLA scaffolds as bioactive platforms for advanced bone tissue engineering applications.

Conflicts of interest

There are no conflicts to declare.

Data availability

Data will be made available on request.

Supplementary information (SI) is available. The supplementary information contains additional mechanical characterization, degradation studies, and the preliminary nanoparticle coating optimization data. See DOI: https://doi.org/10.1039/d6bm00733c.

Acknowledgements

The first author was supported by the Tubitak BIDEB 2211 Scholarship Program. This work was supported by Yeditepe University (Project No. HD-23018). We thank the Arçelik R&D group for producing filaments from Corbion PLA beads, and we extend special thanks to Prof. Çağla Çiçek's team for their invaluable assistance with the animal experiments.

During the preparation of this work, the authors used ChatGPT (OpenAI) to assist with language editing and manuscript structuring. After using this tool, the authors reviewed and edited the content as needed and take full responsibility for the content of the publication.

References

1 T. Ghassemi, A. Shahroodi, M. H. Ebrahimzadeh, A. Mousavian, J. Movaffagh and A. Moradi, *Arch. BONE Jt. Surg.*, 2018, **6**, 90–99.
2 J. O. Hollinger, T. A. Einhorn, B. A. Doll and C. Sfeir, *Bone Tissue Engineering*, CRC Press, London, 2005.
3 A. Gregor, E. Filová, M. Novák, J. Kronek, H. Chlup, M. Buzgo, V. Blahnová, V. Lukášová, M. Bartoš, A. Nečas and J. Hošek, *J. Biol. Eng.*, 2017, **11**, 31.
4 A. Grémare, V. Guduric, R. Bareille, V. Heroguez, S. Latour, N. L'heureux, J.-C. C. Fricain, S. Catros and D. Le Nihouannen, *J. Biomed. Mater. Res., Part A*, 2018, **106**, 887–894.
5 J. Sarukawa, M. Takahashi, M. Abe, D. Suzuki, S. Tokura, T. Furuike and H. Tamura, *J. Biomater. Sci., Polym. Ed.*, 2011, **22**, 717–732.
6 S. Zeng, Z. Cui, Z. Yang, J. Si, Q. Wang, X. Wang, K. Peng and W. Chen, *J. Mater. Sci.*, 2016, **51**, 9958–9970.
7 Z. Wang, K. Wang, X. Lu, M. Li, H. Liu, C. Xie, F. Meng, O. Jiang, C. Li and W. Zhi, *J. Biomed. Mater. Res., Part A*, 2015, **103**, 1520–1532.
8 Y. Parajó, I. D'Angelo, A. Welle, M. Garcia-Fuentes and M. J. Alonso, *Drug Delivery*, 2010, **17**, 596–604.
9 N. İ. Büyük, D. Aksu and G. Torun Köse, *Int. J. Polym. Mater. Polym. Biomater.*, 2022, 1–11.
10 N. İ. Büyük and G. Torun Köse, *Polym. Adv. Technol.*, 2024, **35**, 1–11.
11 W. Chen, L. Nichols, F. Brinkley, K. Bohna, W. Tian, M. W. Priddy and L. B. Priddy, *Mater. Sci. Eng., C*, 2021, **120**, 111686.
12 R. Subbiah, M. P. Hwang, S. Y. Van, S. H. Do, H. Park, K. Lee, S. H. Kim, K. Yun and K. Park, *Adv. Healthcare Mater.*, 2015, **4**, 1982–1992.
13 S. Farah, D. G. Anderson and R. Langer, *Adv. Drug Delivery Rev.*, 2016, **107**, 367–392.
14 T. Furuike, H. Nagahama, T. Chaochai and H. Tamura, *Fibers*, 2015, **3**, 380–393.
15 A. Shanmugavadivu and N. Selvamurugan, *Nanoscale Adv.*, 2025, **7**, 1636–1649.
16 E. Baran and H. Erbil, *Colloids Interfaces*, 2019, **3**, 43.
17 L. R. Jaidev and K. Chatterjee, *Mater. Des.*, 2019, **161**, 44–54.
18 L. Qi, Z. Xu, X. Jiang, C. Hu and X. Zou, *Carbohydr. Res.*, 2004, **339**, 2693–2700.
19 N. Monteiro, A. Martins, R. L. Reis and N. M. Neves, *Regen. Ther.*, 2015, **1**, 109–118.
20 S. Mathews, P. K. Gupta, R. Bhonde and S. Totey, *Cell Prolif.*, 2011, **44**, 537–549.
21 L. Witek, Y. Shi and J. Smay, *J. Adv. Ceram.*, 2017, **6**, 157–164.
22 E. K. Cushnie, B. D. Ulery, S. J. Nelson, M. Deng, S. Sethuraman, S. B. Doty, K. W. H. Lo, Y. M. Khan and C. T. Laurencin, *PLoS One*, 2014, **9**, e101627.
23 L. Chu, G. Jiang, X.-L. Hu, T. D. James, X.-P. He, Y. Li and T. Tang, *J. Mater. Chem. B*, 2018, **6**, 1658–1667.
24 G. Gürel Peközer, N. Abay Akar, A. Cumbul, T. Beyzadeoğlu and G. Torun Köse, *ACS Biomater. Sci. Eng.*, 2021, **7**, 1526–1538.
25 M. Shahrezaee, M. Salehi, S. Keshtkari, A. Oryan, A. Kamali and B. Shekarchi, *Nanomedicine*, 2018, **14**, 2061–2073.
26 B. Cook, R. Rafiq, H. Lee, K. M. Banks, M. El-Debs, J. Chiaravalli, J. F. Glickman, B. C. Das, S. Chen and T. Evans, *Cell Chem. Biol.*, 2019, **26**, 926–935.
27 K. Hu and B. R. Olsen, *Bone*, 2016, **91**, 30–38.
28 C. M. R. Lacerda, *Bone Regen. Concepts, Clin. Asp. Futur. Dir*, 2018, pp. 231–254.
29 R. T. Peterson, S. Y. Shaw, T. A. Peterson, D. J. Milan, T. P. Zhong, S. L. Schreiber, C. A. MacRae and M. C. Fishman, *Nat. Biotechnol.*, 2004, **22**, 595–599.
30 S. Islam, M. S. Ahmed, M. A. Islam, N. Hossain and M. A. Chowdhury, *Results Surf. Interfaces*, 2025, **19**, 100529.
31 A. Stefanache, I. I. Lungu, N. Anton, D. Damir, C. Gutu, A. P. Condratovici, M. Duceac, M. Constantin, G. Calin, L. D. Duceac and M. Boev, *Polymers*, 2025, **17**, 1453.
32 M. Bračič, B. M. Nagy, O. Plohl, F. Lackner, T. Steindorfer, R. C. Fischer, T. Heinze, A. Olschewski, K. S. Kleinschek, C. Nagaraj and T. Mohan, *iScience*, 2024, **24**, 110692.
33 A. Grosso, M. G. Burger, A. Lunger, D. J. Schaefer, A. Banfi and N. Di Maggio, *Front. Bioeng. Biotechnol.*, 2017, **5**, 1–7.
34 A. J. Rennekamp and R. T. Peterson, *Curr. Opin. Chem. Biol.*, 2015, **24**, 58–70.
35 T. N. Sato, *Mechanical and Chemical Signaling in Angiogenesis*, Springer Berlin Heidelberg, Berlin, Heidelberg, 2013, vol. 12.
36 A. F. Wulandari, S. Zulaihah, I. Rachmadanti and A. Aminatun, *AIP Conf. Proc.*, 2020, **2314**(1), DOI: 10.1063/5.0034693.

